Experimental constraints on the fate of H and C during planetary core-mantle differentiation. Implications for the Earth

Valérie Malavergne, Hélène Bureau, Caroline Raepsaet, Fabrice Gaillard, Mélissa Poncet, Suzy Surble, David Sifré, Svyatoslav Shcheka, Chloé Fourdrin, Damien Deldicque, et al.

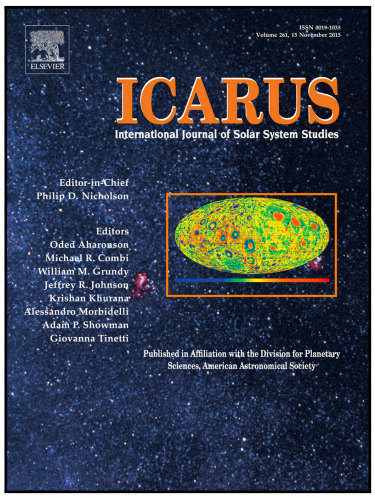

Experimental constraints on the fate of H and C during planetary core-mantle differentiation. Implications for the Earth

Valérie Malavergne , Hélène Bureau , Caroline Raepsaet , Fabrice Gaillard , Mélissa Poncet , Suzy Surblé , David Sifré , Svyatoslav Shcheka , Chloé Fourdrin , Damien Deldicque , Hicham Khodja

PII: S0019-1035(18)30334-8
DOI: https://doi.org/10.1016/j.icarus.2018.11.027
Reference: YICAR 13109

To appear in: *Icarus*

Received date: 16 May 2018
Revised date: 9 November 2018
Accepted date: 26 November 2018

Please cite this article as: Valérie Malavergne , Hélène Bureau , Caroline Raepsaet , Fabrice Gaillard , Mélissa Poncet , Suzy Surblé , David Sifré , Svyatoslav Shcheka , Chloé Fourdrin , Damien Deldicque , Hicham Khodja , Experimental constraints on the fate of H and C during planetary core-mantle differentiation. Implications for the Earth, *Icarus* (2018), doi: https://doi.org/10.1016/j.icarus.2018.11.027

Highlights.

- Our experiments model core formation relevant to telluric planets.
- At high pressures Hydrogen (H) becomes slightly siderophile.
- At high pressures Carbon (C) becomes less siderophile.
- The capacity of a core to retain H or C is controlled by the size of the planet.
- C and H can be present in the Earth's core but H remains a minor element.

Experimental constraints on the fate of H and C during planetary core-mantle differentiation. Implications for the Earth.

Valérie Malavergne[1], Hélène Bureau[2], Caroline Raepsaet[3], Fabrice Gaillard[4], Mélissa Poncet[1], Suzy Surblé[3], David Sifré[4], Svyatoslav Shcheka[5], Chloé Fourdrin[1], Damien Deldicque[6], Hicham Khodja[3].

[1] Université Paris Est Marne La Vallée, Laboratoire des Géomatériaux et Environnement (LGE), Champs-sur-Marne, 77454 Cedex, France.

[2] Institut de Minéralogie, de Physique des Matériaux et de Cosmochimie (IMPMC), Sorbonne Universités – UPMC Université Paris 6, CNRS UMR 7590, Muséum National d'Histoire Naturelle, IRD UR 206, 4 place Jussieu, 75252 Paris Cedex 05, France

[3] LEEL, NIMBE, CEA, CNRS, Université Paris-Saclay, CEA Saclay 91191 Gif-sur-Yvette France

[4] Institut des Sciences de la Terre d'Orléans, Orléans, France.

[5] Bayerisches Geoinstitut, Universität Bayreuth, D-95440, Bayreuth, Germany.

[6] Ecole Normale Supérieure, Laboratoire de Géologie, 24 rue Lhomond, 75005 Paris, France.

*Corresponding author: **Valérie Malavergne, Valerie.Malavergne@u-pem.fr**

Abstract: Hydrogen (H) and carbon (C) have probably been delivered to the **Earth** mainly during accretion processes at High Temperature (*HT*) and High Pressure (*HP*) and at variable redox conditions. We performed *HP* (1 – 15 GPa) and *HT* (1600 – 2300°C) experiments, combined with **state-of-the-art** analytical techniques to better understand the behavior of H and C during planetary differentiation processes. We show that increasing pressure makes H

slightly siderophile and slightly **decreases** the highly siderophile nature of C. This implies that the capacity of a growing core to retain significant amounts of H or C is mainly controlled by the size of the planet: small planetary bodies may retain C in their cores while H may have rather been lost in space; larger bodies may store both H and C in their cores. During the Earth's differentiation, both C and H might be sequestrated in the core. However, the H content of the core would remain one or two orders of magnitude lower than that of C since the $(H/C)_{core}$ ratio might range between 0.04 and 0.27.

Keywords: Planetary differentiation, hydrogen, carbon, core segregation, primitive Earth.

1. Introduction.

Telluric planets formed by accretion of chondritic-like materials. These chondritic materials might contain significant amounts of Hydrogen (H) and Carbon (C) as observed, for example, in carboneous chondrites (*e.g*. Morbidelli *et al*, 2012; Marty, 2012; Yang *et al*, 2016; Iizuka-Oku *et al*, 2017). Unfortunately, the exact nature of the terrestrial precursor materials and the redox conditions at early stages of the Earth formation (*e.g.* Okuchi, 1997; Frost *et al*, 2008; Hirschmann *et al*, 2012 ; Rubie *et al*, 2015) remain uncertain. In case of incomplete devolatilization of the Earth during its accretion (*e.g*. Albarede *et al* 2013; Yang *et al*, 2016; Iizuka-Oku *et al*, 2017; Tikoo and Elkins-Tanton, 2017), the mantle (*e.g*. Frost *et al*, 2008; Yang *et al*, 2016) and possibly the core (*e.g*. Okuchi, 1997; Ohtani *et al*, 2005; Ohtani, 2015; Iizuka-Oku *et al*, 2017) likely trapped H and C. Defouiloy *et al*, (2013) have found around 100 - 200 wt ppb of H in Fe-Ni alloys of iron meteorites, implying that H was present during the formation of their parental body and could potentially enter the core. Results of Hallis *et al* (2015), based on H isotope systematics of Baffin Island and Iceland lavas, showed that the water from the Earth's mantle might have a protosolar nebula origin. In parallel, Marty *et al* (2016) showed that volatiles of the Earth might originate from both the nebular gas and accreting materials. Taken together, all these results suggest that H was not entirely lost during the accretion of the Earth and suggest that a significant amount of H remained stored deep in Earth's interior.

The Earth's core is mainly composed of Fe-Ni alloy, with iron being the major constituent. The addition of ~10% of light elements (S, Si, O, C and H) is required to account for the density deficit observed between pure Fe and core models (*e.g* Poirier, 1994; Chabot *et al*, 2015). It has been shown that H or C can easily be combined with iron at high pressures (*HP*) and high temperatures (*HT*) and could explain such a density deficit (*e.g*. Fukai, 1984 ; Badding *et al*, 1991 ; Yagi and Hishinuma, 1995 ; Wood *et al*, 1996 ; Okuchi, 1997; Saxena

et al, 2004 ; Sakamaki *et al*, 2009 ; Shibazaki *et al*, 2009, 2011 ; Dasgupta *et al*, 2009 ; Dasgupta and Hirschmann, 2010 ; Narygina *et al*, 2011 ; Shibazaki *et al*, 2012, 2014 ; Sakamaki *et al*, 2016 ; Iizuka-Oku *et al*, 2017 ; Dasgupta *et al*, 2013 ; Lord *et al*, 2009 ; Tsuno *et al*, 2018) . **However,** a recent study of Clesi *et al* (2018) showed that H is lithophile **during core – mantle equilibration and it might be a very minor element in the Earth's core. Clesi *et al* (2018) noticed a decrease of the lithophile character of H at *HP-HT* but these conclusions seemed at odds with Okuchi (1997), who observed a clear siderophile behavior for H in a pioneer study**. These conflicting observations imply that we do not have a clear picture on whether H would be siderophile or lithophile at the *P-T*-redox conditions of core formation in a magma ocean.

At the Hadean, the magma ocean might have been extremely reduced (*e.g.* Javoy *et al*, 2010; Rubie *et al*, 2015). Assuming that planetary precursors could be differentiated to some extent and **that** an equilibrium between the proto-core **and primitive** ocean magma might occur during the differentiation (*e.g.* Righter and O'Brien, 2011; Tikoo and Elkins-Tanton, 2017), a wide range of pressures, temperatures and redox conditions should be considered while studying core formation.

Accordingly, the main goals of this study are: (i) to provide new data on the distribution of H and C between the core and the mantle during planetary differentiation at variable pressures, temperatures and redox conditions relevant to magma oceans prevailing on planetary bodies and the primitive Earth, (ii) to evaluate the C and H contents of the Earth's forming core, (iii) to **propose C and H contents for other planetary bodies**.

2. Experimental and analytical procedures.

2.1. Starting materials

Two different synthetic glasses (Tables 1 and 2), a natural brucite $Mg(OH)_2$ and different synthetic metallic alloys (Fe-Ni and Fe-Ni-Si) (Table 1 and 2) were used as starting materials.

The metallic alloys were synthesized and characterized at the Institute of Chemistry and Materials (ICMPE, Créteil, France). The relative proportions of each material (brucite, synthetic glass, metallic alloy) before *HP-HT* experiments, as well as the *P-T-fO₂* conditions are given in Table 2. In order to avoid the massive formation of H-rich bubbles in the metallic phases of our samples, **that was observed in** Okuchi (1997), **we worked at low H contents, and far from the hydride (FeH_x) stability field. FeH_x are known to decompose during the quenching of the experimental charges triggering H_2-bubbles. This process makes the determination of the H content in metal very difficult or impossible.** The H-bearing starting compositions (silicate glass + brucite + metal) were loaded in the graphite capsule by adding small metallic chips to the "silicate+brucite" mix and were weighed in order to obtain the appropriate relative proportion.

2.2. High-pressure and high-temperature experiments.

The lowest pressure experiments (1 GPa) were performed with a piston-cylinder apparatus (non-end loaded) (ISTO, Orleans, France and NASA/LPI, Houston, USA). Each H-bearing sample was **held** in a double capsule: the starting materials were contained in a graphite capsule, which was itself loaded in a Pt capsule. This capsule setup was used in previous studies in order to retain as much H as possible within the samples (*e.g.* Stanley et al, 2014). For the H-free sample, a single graphite capsule was used. The samples were loaded in conventional high-pressure assemblies consisting of a lead sheet, talc-pyrex pressure cell and graphite furnace. The assembly components, except the graphite and Pt parts, were first dried in an oven at 1000°C for 12 hours to remove impurities and later kept in an oven at 150°C. The samples were first pressurized at room temperature and then heated in the range 1400–1700°C for durations ranging from 2 to 30 min (Table 2). The temperature during the experiment was monitored with a B-type thermocouple contained in an alumina ceramic tube. The samples were quenched by switching off the electrical power and the quench rate was

approximately 300°C/s. More details about the experimental setups are given in Sifre *et al.* (2015) and in Malavergne *et al* (2016). The highest pressure experiments (5-15 GPa) were performed in Kawaii-type multianvil presses with tungsten carbide cubes as secondary anvils at the Bayerisches Geoinstitut, Bayreuth, Germany. Pressure calibration curves reported in Tronnes and Frost (2002) were used. Experiments at 5, 6-10 and 15 GPa were carried out with 25/17, 18/11 and 14/8 assemblies (octahedral edge length/truncation edge length in mm), respectively. The pressure assembly consisted of octahedral Cr-doped MgO pressure medium, ZrO_2 sleeve, $LaCrO_3$ heater and MgO sleeve containing the sample capsule. Components of the high-pressure assemblies were fired at 1000°C for 1 hour before experiment to remove moisture. The assembled octahedra were dried in a vacuum oven at 130°C overnight before each experiment. In all experiments the temperature was monitored with an axial $W_3Re/W_{25}Re$ thermocouple. The samples were first compressed to the target pressure within 4 hours and then heated at the rate 100°C/min to the target temperature (1600–2200°C) for durations ranging from 2 to 10 min (Table 2). The temperature uncertainty was estimated to be ±100°C (*e.g*. Agee *et al*., 1995) for the highest temperature experiments. The samples were quenched by switching off the electrical power and the quench rate was approximately 500°C/s. The samples were then decompressed over 12 hours. Because of the use of graphite capsules, our samples are saturated by carbon. This high carbon abundance in our systems does not represent the most relevant chemistry for primitive planetary conditions. However, the choice of these graphite containers for our samples remains one of the best technological solutions to protect them from the rest of the assembly without contaminating reactions. All experimental charges (multianvil and piston-cylinder experiments) were mounted in epoxy resin, sectioned, and polished to reveal the samples. The samples were **analyzed** by all the methods presented below but the ion microprobes. After that, the epoxy resin was removed in

order to avoid any possible H contamination during the nuclear microprobe analysis. The samples were finally mounted in indium.

2.3. Analytical Methods

Scanning Electron Microscope (SEM). A JEOL JSM-5910LV SEM was used for initial evaluation of experiments (at Ecole Normale Supérieure de Paris, France) to determine the homogeneity of phases. SEM investigations were performed at 15 kV accelerating voltage and a working distance of about 8 mm. Qualitative and quantitative chemical analyses were acquired using a Silicon Drift Detector (SDD).

Electron probe microanalyzers (EPMA). A CAMECA SX-100 equipped with wavelength dispersive X-ray spectrometers (WDS) was used to analyze the samples (at CAMPARIS, Jussieu, Paris, France). The oxygen concentrations in the silicate were calculated based on standard valences for the measured major elements: 4+ for Si and Ti; 3+ for Al and Cr; 2+ for Fe, Mn, Mg, Ca; 1+ for Na and K. EPMA were performed with an accelerating voltage of 15 kV and a beam current of 10 or 40 nA with a spot size ranging from around 1 to 10 μm, depending on the analyzed phases. The standards used to analyze the silicates were Fe_2O_3, Fe or olivine for Fe, clinopyroxene for Si, Ca and Mg, $MnTiO_3$ for Mn and Ti, orthoclase for Al and K, NiO for Ni, Cr_2O_3 for Cr, albite for Na. The standards used to analyze the metals were pure Fe, Ni, Cr, Mn and Pt for Fe, Ni, Cr, Mn, Pt and FeSi alloy for Si. The compositions of all phases in our samples are reported in Tables 3. The uncertainty is defined by the ($\sigma/\sqrt{N}$) where σ is the standard deviation of the measurements and N is the number of analyses. The uncertainty is generally less than 3 wt% for major elements and less than 15 wt% for minor elements.

Nuclear microprobe. Ion beam analyses were performed at the nuclear microprobe of Saclay (Khodja *et al.*, 2001) in order to obtain the C and H concentrations in metal and silicate. The spectra of the reaction products (X-rays, charged particles) resulting from the interaction of an

energetic ion beam with the target allowed the determination of the local elemental composition. The approach used to quantify C and H present in our samples requires two different ion beam conditions and analysis techniques. Hydrogen determination was made by Elastic Recoil Detection Analysis (ERDA) (Bureau *et al*, 2009 ; Withers *et al*, 2012 ; Clesi *et al*, 2018). An incident beam of alpha particles was accelerated in order to arrive on the sample (with a size of 12*3 μm^2) with a high energy (3 MeV). The beam ejected the hydrogen atoms of the sample. The spectrum of the H atoms ejected was collected in a 17 mSr Si detector shielded with a 15 µm Al foil. Backscattered alpha particles and X-ray spectra were also used to select the regions of analysis and the relevant phases, silicates or metal as shown in Fig. 1. The H contents are given with an accuracy of about 16wt% for both phases and confirmed by the analysis of well-known silicate glasses from the STR series (Stromboli glasses, Bureau *et al*., 2009). A 1500 keV deuteron microbeam was used to measure the C contents of the metallic and silicate phases thanks to the nuclear reaction $^{12}C(d,p)^{13}C$. A 50 µm Mylar filter stopped backscattered deuterons. Protons generated after incident $^2H^+$ impact with sample were detected at 170° using an annular detector with a solid angle of 110 mSr. All measurements were performed by scanning different areas (between $50 \times 200\ \mu m^2$ to $100 \times 400\ \mu m^2$ depending on samples) by a $3 \times 3\ \mu m^2$ beam. The carbon region (between 2.0 and 2.3 MeV), corresponding to the deep carbon (*i.e*. the carbon without surface contamination), allowed us to determine the real concentration of carbon in metal and silicate phases. As for the ERDA measurements, the elemental X-ray maps allowed the extraction of the ERDA elemental maps, in order to distinguish the metallic and silicate phases. The uncertainty is determined based on **the standard deviations of the standard sample measurements.** The carbon content in metal is given with an accuracy of 4 to 8wt% and the carbon content in silicate is given with an accuracy of 15 to 17wt%. Concentrations are confirmed by the analysis of Certificate Carbon standards from the British Chemical

standards for metal analysis (white cast iron 247/5 with 2.93 wt.% C and carbon steel 215/1 with 0.925 wt% C) and from the silicate glass STR9 (154 ppm C, Bureau *et al*., 2009). Elemental maps of the regions of interest, with sizes ranging from 25*25 to 400*400 μm^2, depending of the method of analysis and the homogeneity of the area have been made. Data analysis was performed using RISMIN (Daudin *et al*., 2003) and SIMNRA (Mayer, 1999) programs.

Secondary Ion Mass Spectrometry (SIMS). In five samples, the H and C contents of the silicate phases were also measured by Secondary Ion Mass Spectrometry (SIMS) at the ion microprobe INSU CNRS national facility, CRPG Nancy (France). The analyses were performed with the Cameca IMS 1270 E7 ion microprobe, with a 2 nA Cs+ primary ion beam focused on a 15 µm diameter area and the electron gun for the charge compensation. The negative secondary ions $^{12}C^-$, $^{17}O^-$, $^{16}OH^-$, $^{27}Al^-$, and $^{30}Si^-$ were measured with a mass resolution of 7000 (M/ΔM). The hydrogen contents determined by this method were exclusively those present as OH^- in the silicates. Before each measurement, the sample was pre-sputtered for 180 seconds with a beam rastering on 15 μm^2 in order to remove sample surface contamination. The measurements were made by ion counting in mono-collection mode (or on Faraday cup for counting rate higher than $3x10^5$ cps) by peak switching with counting time and waiting time of 4s and 2s, respectively, for each peak. 12 successive acquisition cycles were accumulated for each measurement. The H and C concentrations were calculated using the OH^-/Si^- and C^-/Si^- ratios, with Relative Sensitivity Factors (RSF) determined on 4 experimental standard glasses (M35, M40, M43, M48: Shishkina *et al*., 2010). Between three to five points were measured on each sample, and the H and C content are given with an accuracy of about 20%. These contents are reported in the Table 3.

Raman micro-spectrometry. Raman measurements were carried out on a Renishaw INVIA spectrometer equipped with a microscope and a CCD detector (LGE, France). A 532 nm

solid-state green (Nd:YAG) laser was used with a maximal power of 25 mW. The acquisitions were performed through a Leica (x100) magnification objective after a calibration achieved on a silicon standard. The Rayleigh scattering component was removed by an Edge filter. The Raman-scattered light was dispersed by a holographic grating with 1800 lines/mm. The integration time was set at 60 s. The spectra of the pristine glass and the quenched silicate melt of #O2-16 were accumulated 10 and 30 times respectively (Fig. 2a-b). The sample #O2-16 was the only one for which the liquid silicate had quenched as a glass.

2.4. fO_2 calculations.

The oxygen fugacity of the samples was determined relative to the iron-wüstite (*IW*) equilibrium, as in many previous studies (*e.g.* Berthet *et al*., 2009; Dasgupta *et a*l 2013; Chi *et al*, 2014; Li *et al*, 2016; Tsuno et al., 2018), according to the following equation:

$$\Delta IW = \log fO_{2\ experiment} - \log fO_{2\ IW} = 2\log(a_{FeO}/a_{Fe}) \quad (1)$$

with $a_{FeO} = \gamma_{FeO}\, x_{FeO}$ (activity of FeO in the silicate melt), and $a_{Fe} = \gamma_{Fe}\, x_{Fe}$ (activity of Fe in the Fe-rich metallic alloy). For Fe in metallic quenched melts, we used activities values, which incorporated non-ideal interactions amongst the different constituents (Ma, 2001). We calculated the activity of Fe in the metallic melt **(and the interactions between all the elements present in the metal)** using a metal activity calculator (http://norris.org.au/metalact, Norris software) provided by the University of Oxford as in Tsuno *et al* (2018). For FeO in the silicate melt, previous studies (O'Neill and Eggins, 2002; Holzheid *et al*, 1997) showed that the activity coefficient γ_{FeO} is around 1.50. We found fO_2 for our samples ranging from around ΔIW-1.5 (*i.e.* 1.5 log units below the *IW* buffer) down to ΔIW-5.2 (*i.e.* 5.2 log units below the *IW* buffer) (Table 2). A maximum uncertainty of ±0.4 log unit was estimated for these fO_2 calculations. We also did the fO_2 calculations in the ideal solution case (Table 2) and we observed a maximum difference of 0.5 log units with the non-ideal case as in many previous studies (*e.g.* Dasgupta *et al*, 2013; Chi *et al*, 2014).

3. Results.

3.1. Textures and phase assemblages in the samples.

The main phases present in all experimental samples consisted of two quenched immiscible melts: a silicate and a metallic one (Fig. 3). Their compositions are given in Tables 3A-3B. The presence of only two immiscible melts (silicate and metal) in all samples showed that the starting brucite (when present) completely reacted with the silicates after its decomposition into MgO and H_2O-rich fluid during the runs. Periclase and the H_2O-rich fluid reacted with the silicate melt during the experiment. The silicates quenched once to a glass (sample #O2-16) or to an aggregate of tiny dendrites (*e.g.* sample #V527, Fig3b). These dendritic textures are well known and are interpreted as typical quenched structures (*e.g.* Berthet *et al*, 2009). The metallic phases contained very tiny quenched structures as illustrated in Fig. 3. When some brucite was initially present in the runs, then the metallic phases had always few small spherical voids (Fig. 3a). In the runs without brucite, the metallic part of the samples did not exhibit spherical microstructures (Fig. 3b) showing that the presence of hydrogen in the sample was responsible of these textures in the metals. These spherical voids had already been observed in previous studies and were interpreted as possible "bubbles" of H_2 that appeared during the quench of the samples (*e.g.* Okuchi, 1997). Based on SEM high-resolution images, it was possible to measure the ratio $A_{Surfaces}$ of the area occupied by the H_2 bubbles to that of the bubble-free metal. The $A_{Surfaces}$ values ranged between ~0.004 (in the samples M6E2, O1-16, O1-14 and O2-16) and ~0.015 (in the samples B1-10, B2-10 and H4178). As in Okuchi (1997), we took a value of ρ_{H_2}= 0.13 g/cm^3 and we made the assumption that the ratio of the surfaces (bubbles / metal) was similar to the ratio of the volumes (bubbles / metal). For each sample we found a negligible contribution of the H outgassed (between ~0.2 ppm, in the poorest H metal contents of our study, and ~2 ppm in the

highest H one), compared to the H dissolved in metal (between ~20 to ~240 wt ppm, Table 3B). **We therefore decided to neglect the bubble contributions to the H content in metals.** The Raman spectra of the quenched silicate melt of sample #O2-16 is presented in Fig. 2, with a spectrum of the starting anhydrous glass (Fig. 2a) and quenched silicate melt after *HP-HT* reaction (Fig. 2b). These Raman results clearly showed the **presence** of H and C in the quenched silicate melt and the absence of detectable amount of C and H in the majority of anhydrous glasses used as starting materials for all experiments. Based on previous similar studies (*e.g*. Mysen *et al*, 2009; Mysen, 2012; Hirschmann *et al*, 2012; Dasgupta *et al*, 2013; Stanley *et al*, 2014; Kadik *et al*, 2014), we were able to attribute the frequencies characteristic to the vibration of certain atomic groups to the Raman bands: OH stretching (large band at ~3600 cm^{-1}), CH_4 or methyl group (band at ~2900 cm^{-1}), possibly the one caused by C-H stretching in alkyne group (band at ~3290 cm^{-1}), C-O (band at ~2130 cm^{-1}), CO_3^{2-} carbonate (doublets at ~1430 and 1520 cm^{-1}), the characteristic Si-O stretching of silicate glasses (band at ~700 and 900 cm^{-1}) in the silicate melts.

3.2. Major element compositions of the samples.

The compositions of the quenched silicate melts reflected an increase in Mg due to the presence of brucite in some samples after *HP-HT* reactions, but also a strong depletion of Fe in the most reduced samples. The quenched silicate melts had Si and Mg contents varying from about 22 to 31 wt% and from about 13 to 21 wt% respectively (Table 3A). The concentrations of Mg in the silicates are in good agreement with the brucite amounts in the starting mixtures (from 0 up to 2.2 wt%, Table 2). The Fe-content of the quenched silicate **melts of each sample ranged** between 13.60 wt% in the most oxidized run to 0.20 wt% in most reduced one. No compositional gradient was observed either in the quenched silicate melts or in the metallic melts, suggesting that equilibrium was reached before the quench of our experiments. The quenched metallic melts in all runs were Fe-Ni-rich, with Fe

concentrations ranging from about 88 to 94 wt% and Ni from about 1 wt% to 6.5 wt% (Table 3B).

3.4. Carbon and Hydrogen concentrations of the samples.

Carbon was a major element in the metallic melts (with a concentration ranging from 3.4 to 7 wt%) in contrast to silicates where it was a minor element (with a concentration ranging between 0.03 to 0.41 wt% C). At lower Ni content in metal (around 1wt%) the C concentration in metal increased, as already observed by Chi *et al* (2014). The presence of Si in metal seemed to have a negative effect on C as can be seen in the run #M6E2 which contained 2wt% Si and the lowest C content (3.4wt%). The C contents in metal increased slightly with pressure and temperature, while only a small positive pressure effect was observed in silicate. Raman spectroscopy showed that OH^- and CH_4 groups were present in our quenched silicate melts (Fig. 2b). Furthermore, H contents, obtained by SIMS **(sensitive only to OH^-)**, were slightly lower than those measured by ERDA, and supported the presence of CH_4 groups together with hydroxyls in the silicate melts (Table 3A and Fig. 2b). Hydrogen remained a trace element in both metallic and silicate phases (with a concentration ranging between 20 to 236 ppm in metal and between 72 to 1243 ppm in silicate). The H contents in metal increased with pressure. No noticeable pressure or temperature effect on H contents of silicates was observed.

3.5. Attainment of equilibrium in the samples

We argue that all experiments reached equilibrium because:

(1) There were no compositional gradients of the major, minor and trace elements as revealed by multiple analyses (EPMA and SIMS) or mapping (ERDA and NRA) across the silicate and/or metallic melts. The chemical homogeneity of the phases strongly suggested that all the experiments reached equilibrium. Moreover, analysis of the shortest duration runs were consistent with the longest runs (Table 2 and 4).

(2) We performed mass balance calculations in order to check if the samples lost significant H during the *HT-HP* runs or during the quench as suggested by Okuchi (1997). The initial H concentrations before *HT-HP* runs were known (Table 2). The H contents of the recovered samples (after *HP-HT* experiment) were calculated from H analysis in each phase (Tables 3) assuming that the proportions of metal and silicate did not change before and after the *HP-HT* runs. This is confirmed by mass balance of Fe before and after *HP-HT* experiments (Table 2). The results of these mass balance calculations (reported in Table 2) showed that H in our samples did not massively escape.

(3) **The** five data points obtained **for samples at** anhydrous conditions (without brucite) (#4269, #4270, #V527, #SB17 and #SB21, see Table 2) showed a small increase of $D^{Fe}_{metal\text{-}silicate}$ compared to the H-bearing samples synthesized at similar conditions (Table 4). For similar redox and pressure conditions, we observed an increase of ~**30%** at 1 and 10 GPa (at 10 GPa: $D^{Fe}_{metal\text{-}silicate}$ =10 for the H-bearing sample #B1-10, while $\boldsymbol{D^{Fe}_{metal\text{-}silicate}}$ **=13.6** for #4270 (H-free); at 1 GPa: $D^{Fe}_{metal\text{-}silicate}$ =8 for the H-bearing sample #O1-16, while $D^{Fe}_{metal\text{-}silicate}$ = 10 for the H-free sample #SB17). These results are in very good agreement with those of Clesi *et al* (2016) who observed **similar** increase for $D^{Fe}_{metal\text{-}silicate}$ due to H at similar *P*, *T* and fO_2. This increase was **significantly** higher than the error of $D^{Fe}_{metal\text{-}silicate}$ determination and supported **achievement** of equilibrium **during** experiments.

(4) Previous studies at the same experimental conditions (*P* – *T* – run durations) produced equilibrated H-bearing samples (*e.g*. Okuchi, 1997; Dasgupta *et al*, 2013; Stanlay *et al*, 2014; Chi *et al*, 2014; Li *et al*, 2015; Amstrong *et al*, 2015; Clesi *et al*, 2016; Li *et al*, 2016; Clesi *et al*, 2018). **Our $\boldsymbol{D^{H}_{metal\text{-}silicate}}$ are in good agreement with those of Clesi *et al* (2018) (Fig. 4), an internal consistency suggesting equilibrium attainment for both studies.** Accordingly, silicate-liquid diffusion coefficients of major (mainly Si, Mg and O in silicates or Fe and C in metals), minor or trace (H in silicates and metals and C in silicates)

elements vary from ~10^{-7}cm^{2}s^{-1} to ~10^{-4} cm^{2}s^{-1} at the *P-T* of our experiments (*e.g.* Walker and Agee, 1989; Mookherjee *et al*, 2008; Posner *et al*, 2017; Clesi et al 2018). They correspond to characteristic diffusion distances within the range ~ 300 – 800 μm, **indicating that equilibrium attainment should not be impeded by diffusive processes even considering the very short experimental durations.**

Equilibrium in our samples was not only based on the diffusion processes of H and C, but also on the kinetics of oxidation and reduction reactions. In addition, the textural and chemical homogeneity of H and C in both silicates and metallic phases were another argument to demonstrate that chemical equilibrium was reached in the samples of this study.

3.6. Experimental distributions of H between metal and silicate at *HP-HT*.

The partition coefficient $D^H_{metal\text{-}silicate}$ was calculated as the ratio of the H concentration in metal (in wt%) versus the H concentration in silicate (in wt%). The values of $D^H_{metal\text{-}silicate}$ are given in Table 4. The molar partition coefficient $K^H_{metal\text{-}silicate}$ is defined as the ratio of the molar concentration of H in metal versus the molar concentration of H in silicate. Both, $K^H_{metal\text{-}silicate}$ and $D^H_{metal\text{-}silicate}$ can be used in order to understand the distribution of metal and silicate during planetary differentiation. The major difference between $D^H_{metal\text{-}silicate}$ and $K^H_{metal\text{-}silicate}$ is that $D^H_{metal\text{-}silicate}$ can be <1 while $K^H_{metal\text{-}silicate}$ >1 because H is a very light element with respect to the atomic mass of the metal. For example, at 10 GPa, we found $D^H_{metal\text{-}silicate}$ values of 0.5(± 0.1) and 0.33(± 0.07) while their $K^H_{metal\text{-}silicate}$ values were 1.3(± 0.3) and 0.83(± 0.17) respectively. Therefore, at 10 GPa H could be considered as slightly siderophile. **We used $\boldsymbol{D^H_{metal\text{-}silicate}}$ to make mass** balance calculations for primitive Earth and **to allow easier comparison** with previous partitioning studies of different elements between metal and silicate (e.g. Clesi et al, 2018; Dasgupta *et al*, 2013; Stanley *et al*, 2014; Kadik *et al*, 2014). Fig. 4 represents the variation of the partition coefficients of H and C (respectively) between metal and silicate melts $D^H_{metal\text{-}silicate}$ at HP-HT as a function of pressure (*P*), *nbo/t*,

fO_2 and T. The *nbo/t* parameter is the ratio of tetrahedrally coordinated cations (*t*) to nonbridging oxygen ions (*nbo*) (Mysen *et al*, 1985); the larger this ratio is, the less polymerized is the melt. It also helps to understand **a potential effect of the structure of the silicate on** the partition coefficients.

Fig. 4 shows that $D^{H}_{metal\text{-}silicate}$ depends on pressure and to a lesser extent on fO_2 relative to *IW* (ΔIW), T and *nbo/t*. First, the values of $D^{H}_{metal\text{-}silicate}$ increase with pressure at almost constant fO_2 (~ ΔIW-2), from 0.04 at 1 GPa to 0.5 at 10 GPa (Table 4 and Fig. 4); second, $D^{H}_{metal\text{-}silicate}$ can reach 0.22 at 1 GPa at ΔIW-5.2. Therefore, a 10 fold increase in pressure (1 to 10 GPa) makes H more siderophile than a 1000 fold decrease in fO_2 (~ΔIW-1.8 to ΔIW-5.2). **Fig 4c shows that H becomes less lithophile with pressure, and demonstrates siderophile behaviour (meaning $D^{H}_{metal\text{-}silicate}$ >1) at around 15 to 22 GPa.** The partition coefficients calculated from the data of Okuchi (1997) are slightly above 1 at 7.5 GPa and 1500°C while in the present work they are always below 1, increasing with pressure. In Okuchi (1997), experiments were performed without graphite capsule (no C) while our experiments were performed at C saturation. The presence of C may affect the behavior of H at *HP-HT* by decreasing its contents in the metal compared to a C-free system (e.g. Terasaki et al, 2014). Consequently, $D^{H}_{metal\text{-}silicate}$ would be lower in C-saturated system than in a C-free environment (as in Okuchi, 1997).

A multiple linear regression produced the following relation for all the data except the most reduced:

$$\log D^{H}_{metal\text{-}silicate} \ (\pm 0.16) = -4.26^{\pm 1.75} * 1000/T(\mathrm{K}) + 0.18^{\pm 0.03} * 1000 * P(\mathrm{GPa}) / T(\mathrm{K}) - 0.5\ \Delta IW \quad (1)$$

No significant dependence on *nbo/t* was found in this multi-parameter analysis, which is corroborated by independent analysis of the H_2O solubility database in mafic melts (Iacono-Marziano *et al*., 2012). This relationship, where the fO_2 dependence of 0.5 was imposed,

reflects the fact that, close to *ΔIW*-2 **(between *ΔIW*-1 and *ΔIW*-3 from Fig. 4a)**, **H might depend** mainly on the following reaction:

$$OH_{\text{in silicate melt}} \leftrightarrow H_{\text{in metal melt}} + 0.5\ O_2 \quad (2)$$

Under more reducing conditions, ie. *IW*-5.2, the following reaction might mainly characterize the H behavior, **which should, in principle, be fO_2 independent**:

$$H_{2\ \text{in silicate melt}} \leftrightarrow 2\ H_{\text{in metal melt}} \quad (3)$$

Finally, due to the presence of carbon, an inversion of the fO_2 dependence is expected at low fO_2 according to the reactions:

$$CH_{4\ \text{in silicate melt}} + O_2 = CO_{2\ \text{in silicate melt}} + 4H_{\text{in metal melt}} \quad (4)$$

$$\mathbf{CH_{4\ in\ silicate\ melt} + 0.5\ O_2 \leftrightarrow CO_{\text{in silicate melt}} + 4H_{\text{in metal melt}}} \quad \mathbf{(5)}$$

CH_4 is detected in our samples **(Fig. 2)** and Armstrong *et al* (2015) actually described CH_4 as the main H-species at fO_2< IW-3. Eq. (3) implies that the fO_2 dependence at fO_2<*IW*-3 should become inverse and H becomes increasingly lithophile as fO_2 decreases.

Lastly, at graphite saturation, one can consider the following reaction, involving CH_4, where the partitioning of H would not depend on fO_2:

$$\mathbf{CH_{4\ \text{in silicate melt}} \leftrightarrow C_{\text{in metal melt}} + 4H_{\text{in metal melt}}} \quad \mathbf{(6)}$$

These possible trends are qualitatively outlined in fig. 4a, where $D^H_{metal\text{-}silicate}$ that might be controlled by equations (2), (3) and (4) (or (5), (6)) is drawn. More data would be needed to confirm (or not) these hypothesis.

3.7. Experimental distributions of C between metal and silicate at HP-HT.

The partition coefficient $D^C_{metal\text{-}silicate}$ was calculated as the ratio of the C concentration in metal (in wt%) versus the C concentration in silicate (in wt%). The values are given in Table 4. In this work, we measured the Carbon Content at Carbon Saturation (CCCS) in the silicate and metal melts. The partition coefficient of an element between two phases is generally determined when the element is diluted in the system in order to be relevant to geophysical

systems. Previous metallurgical studies have shown a non-ideal behavior of C in Fe-rich alloy liquids (*e.g.* Wang *et al*, 1991) at *HT* showing that above 2.5wt% C, the activity a_C of C was around 3-5 times superior to its C molar fraction X_C. Assuming that such a_C-X_C relationships still hold at high pressure, this implied that the C partition coefficient measured at saturation conditions might be inferior to the $D^C_{metal\text{-}silicate}$ under dilute conditions. Thus, the $D^C_{metal\text{-}silicate}$ determined in our study, as well as in many previous studies (*e.g.* Dasgupta *et al*, 2013; Stanley *et al*, 2014; Chi *et al*, 2014; Li *et al*, 2015; Amstrong *et al*, 2015; Clesi *et al*, 2016; Li *et al*, 2016; Tsuno *et al*, 2018) represented minimum values. Fig. 5 represents the variation of $D^C_{metal\text{-}silicate}$ at HP-HT as a function of pressure (*P*), *nbo/t*, fO_2 and *T*. The C concentrations measured in our samples implied $D^C_{metal\text{-}silicate}$ well above unity (Fig. 5 and Table 4) and in agreement with previous work (Dasgupta *et al*, 2013; Stanlay *et al*, 2014, Chi and Dasgputa, 2014) performed under C saturation conditions. This reflects the strong siderophile affinity of C at these *P*-*T*-redox conditions. Two trends can be highlighted: (i) an increase of $D^C_{metal\text{-}silicate}$ with a decrease of fO_2 (Fig. 5a) and (ii) a decrease of $D^C_{metal\text{-}silicate}$ with an increase of pressure (Fig. 5b). The negative value of the slope for Fig. 5a is ~ -0.5. This value corresponds to the average valence state of 2 for C in silicate (*e.g.* Chi and Dasgputa, 2014**), which may be summarized by the following reaction:**

$$\mathbf{CO_{\ in\ silicate\ melt} \leftrightarrow 0.5\ O_2 + C_{\ in\ metal\ melt}} \quad \mathbf{(7)}$$

A multiple linear regression gave the following relation for our data:

$$\log D^C_{metal\text{-}silicate}\ (\pm 0.4) = 1.70^{\pm 0.65} * 1000/T(\mathrm{K}) - 0.14^{\pm 0.07} * 1000 * P(\mathrm{GPa}) / T(\mathrm{K}) - 0.5\ \Delta IW \quad \mathbf{(8)}$$

No significant dependence on *nbo/t* was found in this multi-parameter analysis with our data. **However, below *IW*-3, the relation (7) should not be used anymore as the behavior of C at lower fO_2 might change due to the formation of CH_4 (*e.g.* reactions (4) or (5) or (6)) as suggested by our Raman results.** Equation (1) and (5) must be seen as empirical fit that can be used for interpolation of our experimental data remaining within a restricted range of *nbo/t*

and total H content. Calculations of H and C partitioning can conservatively be conducted up to 15 GPa, the maximum experimental pressure of our study, while a thorough error propagation formalism must be considered for *P* calculation up to 20 GPa. All statistical uncertainties are provided in equation (1) and (5). For some runs without brucite in the starting material, a small increase of the $D^{C}_{metal\text{-}silicate}$ was observed compared to the H-bearing samples obtained at similar conditions. This increase, even small, remained significant because it was greater than the error on $D^{C}_{metal\text{-}silicate}$. For similar redox and pressure conditions, we observed a 57% decrease of the partition coefficient for H-bearing samples compared to those of H-free samples ($D^{C}_{metal\text{-}silicate}$ =10.6 in #B1-10 against $D^{C}_{metal\text{-}silicate}$ =30.7 for #4270 at 10GPa, and $D^{C}_{metal\text{-}silicate}$ =27 for H-bearing sample #4178 against $D^{C}_{metal\text{-}silicate}$ =63 in the H-free sample #V527 at 5-6GPa). The increase of $D^{C}_{metal\text{-}silicate}$ under anhydrous conditions is much more pronounced in the present study than in previous works (Dasgupta *et al*, 2013).

4. Discussion.

From the partition coefficients of H and C between metal and silicate melts at *HP-HT* and at different fO_2, we show:

(i) a decrease of the lithophile behavior of H at *HP-HT* (Fig. 4).

(ii) H might become siderophile at ~15GPa (Fig. 4).

(iii) a decrease of the siderophile character of C with an increase of pressure (Fig. 5).

(iv) The presence of H might slightly decrease $D^{C}_{metal\text{-}silicate}$ at *HP-HT*.

Below, we discuss two additional points:

(i) due to the decrease of the siderophile nature of C at *HP-HT* and a decrease of the lithophile affinity of H, a strong decrease of the (C/H) ratio **must** be observed during the segregation of a planetary core (**see** Fig. 6).

(ii) H might be a minor element in the Earth's core.

4.1. Hydrogen in planetary cores.

It has been proposed that the main part of H remained in the **Earth's interior** during **its** differentiation (*e.g*. Hirschmann *et al*, 2012 ; Sarafian *et al*, 2014; Hallis *et al*, 2015; Tikoo and Elkins-Tanton, 2017). **In order to test** this hypothesis, we can use our experimental results to calculate how much H might enter the growing core through *HP-HT* metal-silicate melts equilibrium processes (*e.g.* Righter *et al*, 2010, with $P_{equilibrium}$ ~20 GPa, between 1600-2500K and around ΔIW-2 – ΔIW-5). From the possible H contents of the primitive mantle (ranging between ~110, ~300 ppm or ~600 ppm; *e.g*. Marty, 2012; Albarede *et al*, 2013; Rubie *et al*, 2015), we can estimate ranges of H that could enter the forming core:

$$\sim 0.0005 \text{ wt\%} \leq H_{\text{ in Earth's core}} \leq \sim 0.3 \text{ wt\%}.$$

These estimations of H contents might increase if the metal-silicate melts equilibrium process took place at higher pressures (~40-60 GPa) as proposed in recent models (*e.g.* Siebert *et al*, 2012). According to Terasaki *et al* (2012) and Narygina *et al* (2011), about 1 to 1.3 wt% H in the core would be enough to account for all the density deficit of the terrestrial outer core. Our results suggest that H would not be the major light element of the core. Indeed, it would be necessary to have at least ~2.5 – 3.5 wt% of water (or ~ 0.3-0.4 wt% H) in the primitive bulk Earth **to build a core containing 1% H**. Such high H contents could be delivered by some undifferentiated water-rich planetary embryos as, for example, the parent bodies of the CM and/or CI chondrites for example (between 13 to 18 wt% of CI or between 20 to 27 wt% of CM), or by other differentiated water-rich embryos, like Ceres, the largest object in the asteroid belt, which might contain up to 50 vol% of water (Park *et al*, 2016). Finally, the largest hydrous planetary bodies present in the solar nebula (e.g. Hallis et al, 2012; Rubie at al, 2015; Park et al, 2016) could then segregate a core with H contents **approaching up to ~0.5 wt%** depending on their exact size and their H primitive mantle contents. In contrast, for the smallest hydrous planetary bodies (with a central pressure less than ~15 GPa), H would

partition in the magma ocean and/or be lost in space by H_2O degassing (*i.e*. Gaillard and Scaillet, 2014).

4.2. Carbon in planetary cores.

We estimated the C amounts that might enter into the Earth's forming core through metal-silicate melts equilibrium processes (with $P_{equilibrium}$ ~20 GPa, between 1600-2500K and at fO_2 within the range ΔIW-2 – ΔIW-5) with a C content for the primitive mantle deduced from different models of the literature ranging between ~20 or ~300 ppm (*e.g*. Hirschmann and Dasgupta, 2009). We found the following range of values:

$\sim 0.06\ wt\% \leq C_{\text{in Earth's core}} \leq \sim 8\ wt\%$ (solubility limit, *e.g.* Chi and Dasgupta, 2014).

These values might decrease at higher pressures. **Whether the Earth's core could incorporate C to its solubility limit (ie. the CCCS) is discussed below and the consequence of accretion at C-undersaturated conditions is discussed in section 3.7.** The decrease of the siderophile nature of C at *HP-HT* has important implications for early planetary differentiation. If hydrous or anhydrous small planetary bodies were present in the solar nebula (e.g. Hallis et al, 2012; Rubie at al, 2015), then they might segregate a core with high C contents (up to 3-5 wt%). The cores of the biggest bodies would contain less C than the small ones. The most reduced small planetary bodies (Mercury-like bodies) might also sequester high amounts of C in their cores (theoretically close to C solubility limit, depending on the size and the exact redox conditions of the body) except if silicon (Si), due to very low fO_2, entered the core (e.g. Malavergne et al, 2010, 2014). Indeed, it has been shown that the presence of Si in Fe-Ni-C alloys greatly decreases the concentration of C in metal, and can lower the C solubility by a factor 3 (*e.g.* Li *et al*, 2016). **Such effect can also be expected if a realistic amount of S enters the Earth's core composition. Li et al (2016) have shown that a few wt% of S reduces by a factor 5 the carbon content at graphite saturation.** Finally, the presence of H might **slightly** decrease the C contents of these planetary cores. The

decrease would be enhanced with the size of the body as the siderophile nature of C decrease at *HP-HT.* **All in all, planetary accretion and core-mantle segregations at conditions close to carbon saturation may be a hypothesis, justifying that we do not consider here the effects of C dilution in metal on the $D^{C}_{metal\text{-}silicate}$.**

4.3. The cross fate of H and C during planetary differentiation.

We **assume** the Primitive Mantle (PM) contents of C (between 20 and 300 ppm, *e.g.* Hirschmann and Dasgupta, 2009) and H (between 110 and 600 ppm, *e.g.* Marty, 2012; Albarede *et al*, 2013; Rubie *et al*, 2015) by using models found in the literature. The variations of $\frac{D^{H}_{metal-silicate}}{D^{C}_{metal-silicate}}$ ratio as a function of pressure, temperature and fO_2 **(between *IW*-1 and *IW*-3)** can be deduced by our experimental data. This $\frac{D^{H}_{metal-silicate}}{D^{C}_{metal-silicate}}$ ratio showed an **obvious** trend only with pressure (Fig. 6). More data are clearly needed to deduce the variations of this ratio with temperature or fO_2. These ratios ranged from values ~0.0003 at 1 GPa to ~0.04 at 10 GPa. Assuming the following equation:

$$\left(\frac{H_{core}}{C_{core}}\right)=\left(\frac{D^{H}_{metal-silicate}}{D^{C}_{metal-silicate}}\right)\times\left(\frac{H_{PM}}{C_{PM}}\right) \qquad \textbf{(9),}$$

we estimated possible ranges of $\left(\frac{H_{PM}}{C_{PM}}\right)$ and we deduced the possible (H/C) ratios during the core segregation for 1-10 GPa and variable fO_2:

$$0.03 \leq \left(\frac{H_{core}}{C_{core}}\right) \leq 0.27 \qquad \textbf{(10)}$$

The Earth's core must contain other light elements: around 3-7 wt% Si, 2-4 wt% O and 1-3 wt% S (*e.g.* Rubie *et al*, 2015; Fischer *et al*, 2015). The contents of H and C would depend on the oxidized or reduced environment of the primitive Earth during the segregation of the core. Based on this study and on current models (*e.g.* Rubie *et al*, 2015; Righter *et al*, 2011), we can describe the cross fate of H and C during terrestrial differentiation which might **have first**

undergone reduced fO_2 conditions that became **increasingly** oxidized. If terrestrial accretion began under very reducing conditions (between ΔIW-3 and ΔIW-5), the distribution of C would be strongly in favor of the metal of the core at the detriment of the mantle. For the lowest fO_2, **however,** silicon (Si) could be easily combined with the core (*e.g.* Malavergne *et al*, 2014**). The presence of Si in metal might decrease the C contents of the core** (*e.g.* Li *et al*, 2015). **Thus, low fO_2 might strengthen the decrease of the highly siderophile nature of C**. H would become increasingly siderophile with increasing depths (corresponding to pressure values of 15-22 GPa) in the magma ocean of the proto-planet. Moreover, the results of Iizuka-Oku *et al* (2017), suggest that H might no longer be a trace element in the cores of small differentiated bodies, which might be part of the Earth's accretion. The siderophile character of C would gradually decrease as pressure increased. For the Earth, we found that the H contents in the core might range between ~0.0005 wt% and ~0.3 wt%. We could then determine possible ranges for C in the Earth's forming core using the relation (9). We proposed that the C content may have minimum values of ~0.6 - 1 wt% and maximum values around ~2.4 wt%. Finally, our work showed that the metallic core might store H and C **throughout** its formation.

The differentiation of smaller planetary bodies in the primitive solar nebula would **impact** the (H/C) fractionation **differently from Earth's size body**. As the ratio $\frac{D^{H}{}_{metal-silicate}}{D^{C}{}_{metal-silicate}}$ is increasing with pressure, H and C would be more and more fractionated during the growth of the body. The degree of (H/C) fractionation of planetary materials (as chondrites and achondrites for example) could thus be an indirect indicator of the size of the planetary body. The smallest bodies **(like Vesta for example)** would have the highest (H/C) ratio while the bigger bodies **(*e.g.* like the Moon for example)** the lowest. The cores of the smallest planetary bodies would then contain only traces of H unlike C, which could exceed several wt% (but always less than 7-8 wt%). The cores of **the Earth's size** planetary bodies might

well reach up to ~**0.5** wt% H, levels which might be more comparable with **possible contents** of C.

5. Conclusion.

We have experimentally determined the partition coefficients of H and C between metal and silicate melts between 1–15 GPa, 1600–2200°C and *ΔIW*-2 – *ΔIW*-5.5. Our results showed that increasing pressure makes H less lithophile and C slightly less siderophile. We proposed that the capacity of a planet or a planetary body to keep H and C in the core would be controlled by *HP-HT* equilibration processes at the depth of the core - magma ocean boundary. The smallest cores would retain most of the C whereas H would partition in the magma ocean and/or be lost in space. The cores in the largest planets, like the Earth, would store both H and C, but *HP-HT* equilibration should enable the mantle to retain a significant part of H and C. In the Earth's core, the H content might reach a maximum value of ~0.3 wt% and at least a few tens of ppm, while the C content could reach ~2.4 wt% in the most favorable scenario.

Acknowledgments: This study was partly funded by the German Science Foundation via Core Facility Programme of the Bayerisches Geoinstitut (Germany). We are grateful to the BGI staff for their constant availability and more especially to H. Schulze for his help during sample preparation and Dan Frost for fruitful discussions. The authors wish to thank the nuclear microprobe committee for accepting the project. We are also grateful to Didier Guillier and Yvan Kilisky for the accelerator operation. The authors wish to thank the CRPG ion microprobe committee for accepting the project. We are also grateful to Nordine Bouden and Etienne Deloule for the SIMS analysis. Valerie Paul Boncour and Jean-Marc Joubert from the Institute of Chemistry and Materials (ICMPE, Créteil, France) are thanked for their help and assistance during the alloys synthesis and their characterizations.

References.

Agee C. B., Li J., Shannon M. C., and Circone S., 1995. Pressure- temperature phase diagram for the Allende meteorite. J. Geophys. Res., 100, 17725–17740.

Albarede F., Ballhaus C., Blichert-Toft J., Lee C.-T., Marty B., Moynier F. and Yin Q.-Z., 2013. Asteroidal impacts and the origin of terrestrial and lunar volatiles. Icarus 222, 44–52.

Armstrong, L. S., Hirschmann, M. M., Stanley, B. D., Falksen, E. G. & Jacobsen, S. D., 2015. Speciation and solubility of reduced C-O-H-N volatiles in mafic melt: implications for volcanism, atmospheric evolution, and deep volatile cycles in the terrestrial planets. Geochim. Cosmochim. Acta 171, 283-302.

Asahara Y., Kubo T., Kondo T., 2004. Phase relations of a carbonaceous chondrite at lower mantle conditions, Phys. Earth Planet. Interiors, 143, 421-432.

Badding, J.V., Hemley, R.J., Mao, H.K., 1991. High-pressure chemistry of hydrogen in metals: in situ study of iron hydride. Science 253, 421–424.

Berthet S., Malavergne V., Righter K., 2009. Evolution of Indarch (EH4 chondrite) at 1 GPa and high temperature: implications for early planetary differentiation processes. Geochim Cosmochim Acta 73, 6402-6420.

Bouhifd M.A., Gautron L., Bolfan-Casanova N., Malavergne V., Hammouda T., Andrault D., Jephcoat A.P., 2007, Potassium partitioning into molten iron alloys at high-pressure: Implications for Earth's core, Phys. Earth Planet. Int., 160, 22–33

Bureau H., Raepsaet C., Khodja H., Carraro A., Aubaud C., 2009. Determination of hydrogen content in geological samples using Elastic Recoil Detection Analysis (ERDA). Geochimica et Cosmochimica Acta.

Chabot N.L., Wollack E.A., Humayun M., Shank E.M. 2015. The effect of oxygen as a light element in metallic liquids on partitioning behavior. Meteorit. Planet. Sci. 50, 530–546.

Chi H., Dasgupta R., Duncan M. S., Shimizu N., 2014. Partitioning of carbon between Fe-rich alloy melt and silicate melt in a magma ocean – implications for the abundances and origins of volatiles in Earth, Mars and Moon. Geochim. Cosmochim. Acta 139, 447–471.

Clesi V., Bouhifd M.A., Bolfan-Casanova N., Manthilake G., Fabbrizio A., Andrault D., 2016. Effect of H_2O on metal-silicate partitioning of Ni, Co, V, Cr, Mn and Fe: implication for the oxidation state of the Earth and Mars, Geochim. Cosmo. Acta 192, 97-121.

Clesi V., Bouhifd M.A., Bolfan-Casanova N., Manthilake G., Schiavi F., Raepsaet C., Bureau H., Khodja H., Andrault D., 2018. Low hydrogen contents in the cores of terrestrial planets, Sci. Adv. 4, e1701876.

Dasgupta R., Buono A., Whelan G. and Walker D., 2009. High pressure melting relations in Fe–C–S systems: Implications for formation, evolution, and structure of metallic cores in planetary bodies. Geochim. Cosmochim. Acta 73(21), 6678–6691.

Dasgupta R. and Hirschmann M. M., 2010. The deep carbon cycle and melting in Earth's interior. Earth Planet. Sci. Lett. 298, 1–13.

Dasgupta R., Chi H., Nobumichi S., Buono A. S. and Walker D., 2013. Carbon solution and partitioning between metallic and silicate melts in a shallow magma ocean: implications for the origin and distribution of terrestrial carbon. Geochim. Cosmochim. Acta 102, 191–212.

Daudin L., Khodja H., Gallien J. P. (2003). Development of "position-charge-time" tagged spectrometry for ion beam microanalysis. Nucl. Instrum. Methods Phys. Res. B 210, 153–158.

Defouiloy C., Duhamel R., Robert F., 2013, Ion Microprobe Determination of Hydrogen Concentration and Isotopic ratio in Extraterrestrial Metallic Alloys, Geostandards Geoanakytical Res. 37, 417-427.

Fischer R.A., Campbell A.J., Reaman D.J., Miller N.A., Heinz D.L., Dera P., Prakapenka V.B., 2013, Phase relation in the Fe-FeSi system at high pressures and températures, Earth Planet. Sci. Letters. 373, 54-64.

Frost D. J. and McCammon Catherine A. , 2008. The Redox State of Earth's Mantle. Annual Review of Earth and Planetary Sciences, 36: 389-420.

Fukui H., Inoue T., Yasui T., Katsura T., Funakoshi K.-I., Ohtaka O., 2005. Decomposition of brucite up to 20 GPa: evidence for high MgO-solubility in the liquid phase, Eur. J. Mineral., 17, 261-267.

Gaillard F., Scaillet B. 2014. A theoretical framework for volcanic degassing chemistry in a comparative planetology perspective and implications for planetary atmospheres, Earth Planet. Sci. Letters. 403, 307-316.

Hallis L.J., Huss G. R., Nagashima K., Taylor G. J., Halldórsson S. A., Hilton D. R., Mottl M. J., Karen J. Meech K. J. 2015. Evidence for primordial water in Earth's deep mantle, Science 350, 795-797.

Hirschmann M.M., Withers A.C., Ardia P., Foley N.T. 2012, Solubility of molecular hydrogen in silicate melts and consequences for volatile evolution of terrestrial planets, Earth Planet. Sci. Letters, 345–348, 38-48.

Hirschmann M. M. and Dasgupta R., 2009. The H/C ratios of Earth's near-surface and deep reservoirs, and consequences for deep Earth volatile cycles. Chem. Geol. 262, 4–16.

Holzheid A., Palme H. and Chakraborty S. 1997, The activities of NiO, CoO and FeO in silicate melts. Chem. Geol. 139, 21–38.

Iacono-Marziano G., Morizet Y., Le-Trong E., Gaillard F., 2012. New experimental data and semi-empirical parameterization of H_2O-CO_2 solubility in mafic melts. Geochim. Cosmochim. Acta 97, 1-23.

Javoy M., Kaminski E., Guyot F., Andrault D. Sanloup C., Moreira M., Labrosse S., Jambon A., Agrinier P., Davaille A., and Jaupart C., 2010. The chemical composition of the Earth: enstatite chondrite models. Earth Planet. Sci. Lett. 293, 259–268.

Kadik A. A., Koltashev V.V., Kryukova E.B., Plotnichenko V. G., Tsekhonya T.I., Kononkova N. N., 2014. Solution behavior of C-O-H volatiles in FeO-Na2O-Al2O3-SiO_2 melts in equilibrium with liquid iron. And graphite at 4 GPa and 1550°C. Geochem. Int. 52, 707–725.

Khodja, H., Berthoumieux, E., Daudin, L., and Gallien, J.-P., 2001. The Pierre Süe Laboratory nuclear microprobe as a multi-disciplinary analysis tool. Nucl. Instrum. Methods Phys. Res. Sect. B Beam Interact. Mater. At. 181, 83–86.

Li Y., Dasgupta R., Tsuno K., Monteleone B., Shimizu N., 2016, Carbon and Sulfur budget of the silicate Earth explained by accrétion of differentiated planetary embryos, Nature Geoscience, 9, 781-785.

Li, J., Agee, C.B., 2001b. The effect of pressure, temperature, oxygen fugacity and composition of nickel and cobalt between liquid Fe–Ni–S alloy and liquid silicate: implications for the earth's core formation. Geochim. Cosmochim. Acta 65, 1821-1832.

Iizuka-Oku R., Yagi T., Gotou H., Okuchi T., Hattori T., Sano-Furukawa A. 2017. Hydrogenation of iron in the early stage of Earth's evolution. Nature Commun. 8, 14096 doi:10.1038/ncomms14096.

Lord O. T., Walter M. J., Dasgupta R., Walker D. and Clark S. M., 2009. Melting in the Fe–C system to 70 GPa. Earth Planet. Sci. Lett. 284, 157–167.

Ma Z., 2001. Thermodynamic description for concentrated metallic solutions using interaction parameters. Metall. Mater. Trans. B 32, 87–103.

Malavergne V., Charon E., Jones J., Cordier P., Righter K., Deldicque D., Hennet L. 2016, The formation of nanonuggets of highly siderophile elements in quenched silicate melts at high temperature: before or during the silicate quench?, Earth Planet. Sci. Lett., 434, 197-207.

Malavergne V, Cordier P., Righter K., Brunet F., Zanda B, Addad A., Smith T., Bureau H., Surblé S., Raepsaet C., Charon E., 2014. How Mercury can be the most reduced terrestrial planet and still store iron in its manthe, Earth Planet. Sci. Lett., 394, 186-197.

Malavergne V, Toplis M., Berthet S., J. Jones, 2010, Highly reducing conditions during core formation on Mercury: Implications for internal structure, the distribution of heat-producing elements and the origin of a magnetic field., Icarus, 206, 199-209.

Malavergne V., Tarrida M., Combes R., Bureau H., Jones J. and Schwandt C. 2007, New high-pressure and high-temperature metal/silicate partitioning of U and Pb: implications for the cores of the Earth and Mars. Geochim. Cosmochim. Acta 71, 2637–2655.

Marty B., Avice G., Sano Y., Altwegg K., Balsiger H., Hässig M., Morbidelli A., Mousis O., Rubin M. 2016, Origins of volatile elements (H, C, N, noble gases) on Earth and Mars in light of recent results from the ROSETTA cometary mission, Earth Planet. Sci. Lett. 441, 91-102.

Marty B., 2012. The origins and concentrations of water, carbon,nitrogen and noble gases on Earth. Earth Planet. Sci. Lett. 313–314, 56–66.

Mayer M. (1999). SIMNRA, a simulation program for the analysis of NRA, RBS and ERDA. AIP Conf. Proc. 475, 541–544 10.1063/1.59188.

Mookherjee M., Stixrude L., Karki B., 2008. Hydrous silicate melt at high pressure. Nature, 452 (7190), 983–986

Morbidelli A., Lunine J.I., O'Brien D.P., Raymond S.N., and Walsh K.J., 2012. Building Terrestrial Planets. Annu. Rev. Earth Planet. Sci. 2012. 40:251–75.

Mysen B.O., Virgo D., Seifert F.A. (1985) Relationships between properties and structure of aluminosilicate melts. Am. Mineral. 70, 88-105.

Mysen, B.O., Fogel M.L., Morrill P.L., Cody G.D., 2009. Solution behavior of reduced C-O-H volatiles in silicate melts at high pressure and temperature. Geochim. Cosmochim. Acta 73, 1696–1710.

Mysen B. O., 2012. Silicate-COH melt and fluid structure, their physicochemical properties, and partitioning of nominally refractory oxides between melts and fkuids. Lithos 148, 228-246.

Narygina, O., Dubrovinsky, L.S., McCammon, C.A., Kurnosov, A., Kantor, I.Y., Prakapenka,

V.B., Dubrovinskaia, N.A., 2011. X-ray diffraction and Mössbauer spectroscopy study of fcc iron hydride FeH at High pressures and implications for the composition of the Earth's core. Earth Planet. Sci. Lett. 307, 409–414.

O'Neill H. S. C. and Eggins S. M., 2002. The effect of melt composition on trace element partitioning: an experimental investigation of the activity coefficients of FeO, NiO, CoO, MoO_2 and MoO_3 in silicate melts. Chem. Geol. 186, 151–181.

Ohtani, E., 2015. Hydrous minerals and the Storage of water in the deep mantle. Chem. Geol. 418, 6-15.

Ohtani, E., Hirao, N., Kondo, T., Ito, M., Kikegawa, T., 2005. Iron–water reaction at high pressure and temperature, and hydrogen transport into the core. Phys. Chem. Miner. 32, 77–82.

Okuchi T., 1997. Hydrogen partitioning into molten iron at high pressure: implications for Earth's core. Science 278, 1781–1784.

Park R.S., Konopliv A.S., Bills B.G., Rambaux N., Castillo-Rogez J.C., Raymond C.A., Vaughan A.T., Ermakov A.I., Zuber M.T., Fu R.R., Toplis M.J., Russell C.T., Nathues A., Preusker F., 2016. A partially differentiated interior for Ceres deduced from its gravity field and shape. Nature 537, 515–517.

Poirier J. P., 1994, Light elements in the Earth's outer core : a critical review, Phys Earth Planet. Interiors, 85, 319-337.

Posner E. S., Rubie, D. C., Frost D. J , Steinle-Neumann G., 2017. Experimental determination of oxygen diffusion in liquid iron at high pressure, Earth Planet. Sci. Lett. 464,116-123.

Righter K., O'Brien D.P., 2011. Terrestrial planet formation. Proc. Nat. Acad. Sci. USA 108, 19165-19170.

Righter K., Pando K.M., Danielson L, Cin-Ty L., 2010. Partitioning of Mo, P and other siderophile elements (Cu, Ga, Sn, Ni, Co, Cr, Mn, V and W) between metal and silicate melt as a function of temperature and silicate melt composition, Earth Planet. Sci. Lett. 291,1-9.

Rubie D., Jacobson S., Morbidelli A., O'Brien D., Young E., de Vries J., Nimmo F., Palme H. and Frost D. 2015, Accretion and differentiation of the terrestrial planets with implications for the compositions of early-formed Solar System bodies and accretion of water. Icarus 248, 89–108.

Sarafian A. R., Nielsen S.G., Marschall H. R., McCubbin F. M., Monteleone B. D., 2014. Early accretion of water in the inner solar system from a carbonaceous chondrite-like source. Science, 346, 623-626.

Sakamaki K., Ohtani E., Fukui H., Kamada S., Takahashi E., Sakairi T., Nakajima Y., Takahata A., Sakai T., Tsutsui S., Ishikawa D., Shiraishi R., Seto Y., Tsuchiya T., Baron A.Q.R.., 2016. Constraints on Earth's inner core composition inferred from measurements of the sound velocity of hcp-iron in extrême conditions. Sci. Adv. 2, e1500802.

Sakamaki K., Takahashi E., Nakajima Y., Nishihara,Y., Funakoshi K., Suzuki T., Fukai,Y., 2009. Melting phase relation of FeHx up to 20 GPa: implication for the temperature of the Earth's core. Phys. Earth Planet. Inter. 174, 192–201.

Saxena S. K., Liermann H-P., Shen G., 2004. Formation of iron hydride and high-magnetite at high pressure and temperature. Physics of the Earth and Planetary Interiors 146 313–317.

Shibazaki Y., Ohtani E., Hiroshi F., Sakai T., Kamada S., Ishikawa D., Tsutsui S., Baron A.Q.R., Nishitani N., Hirao N., Takemura K., 2012. Sound velocity measurements in dhcp-FeH up to 70 GPa with inelastic X-ray scattering: Implications for the composition of the Earth's core. Earth Planet. Sci. Lett. 313–314, 79–85.

Shibazaki Y., Ohtani E., Terasaki H., Tateyama R., Sakamaki T., Tsuchiya T., Funakoshi K., 2011. Effect of hydrogen on the melting temperature of FeS at high pressure: implications for the core of Ganymede. Earth Planet. Sci. Lett. 301, 153–158.

Shibazaki, Y., Ohtani, E., Terasaki, H., Suzuki, A., Funakoshi, K., 2009. Hydrogen partitioning between iron and ringwoodite: implications for water transport into the Martian core. Earth Planet. Sci. Lett. 287, 463–470.

Shibazaki Y., Terasaki H., Ohtani E., Tateyama R., Nishida K., Funakoshi K., Higo Y., 2014. High-pressure and high-temperature phase diagram for $Fe_{0.9}Ni_{0.1}$-H alloy. Earth Planet. Sci. Lett. 228, 192-201.

Shishkina T.A., Botcharnikov R.E., Holtz F., Almeev R.R., Portnyagin M.V., 2010. Solubility of H_2O- and CO_2-bearing fluids in tholeiitic basalts at pressures up to 500 MPa, Chemical Geology, 277, 115–125.

Siebert J., Badro J., Antonangeli D., Ryerson F.J., 2012. Metal-silicate partitioning of Ni and Co in a deep magma ocean, Earth Planet. Sci. Lett. 321, 189-197.

Siebert J., Malavergne V., Guyot F., Combes R. et Martinez I., 2004, the behaviour of sulphur in metal-silicate core segregation experiments under reducing conditions, Phys. Earth Planet. Int.,144, p. 421-432.

Sifre D., Hashim L., Gaillard F., 2015. Effects of temperature, pressure and chemical compositions on the electrical conductivity of carbonated melts and its relationship with viscosity. Chem. Geol., 418, 189-197.

Stanley B. D., Hirschmann M. M. and Withers A. C., 2014. Solubility of C–O–H volatiles in graphite-saturated martian basalts. Geochim. Cosmochim. Acta 129, 54–76.

Terasaki, H., Shibazaki Y., Nishida K., Tateyama R., Takahashi S., Ishii M., Shimoyama Y., Ohtani E., Funakoshi K., Higo Y., 2014. Repulsive nature for hydrogen incorporation to Fe_3C up to 14 GPa. ISIJ International 54, 2637–2642.

Terasaki, H., Ohtani E., Sakai T., Kamada S., Asamuma H., Shibazaki Y., Hirao N., Sata N., Ohishi Y., Sakamaki T., Suzuki A., Funakoshi K., 2012. Stability of Fe–Ni hydride after the reaction between Fe–Ni alloy and hydrous phase (δ-AlOOH) up to 1.2 Mbar: Possibility of H contribution to the core density deficit. Phys. Earth Planet. Inter. 194–195,18–24.

Tikoo SM, Elkins-Tanton LT. 2017 The fate of waterwithin Earth and super-Earths and implications for plate tectonics. Phil. Trans. R. Soc. A. 375, 20150394. http://dx.doi.org/10.1098/rsta.2015.0394

Tronnes R. G. and Frost D. J. (2002) Peridotite melting and mineralmelt partitioning of major and minor elements at 22–24.5 GPa. Earth Planet. Sci. Lett. 197, 117–131.

Tsuno K., Grewal D. S., Dasgupta R. (2018) Core-mantle fractionation of carbon in Earth and Mars : the effects of sulfur. Geochim. Cosmochim. Acta 238, 477-495.

Walker D. and Agee C. B., 1989. Partitioning ‘‘equilibrium’’, temperature gradients, and constraints on Earth differentiation. Earth. Planet. Sci. Lett. 96, 49–60.

Wang C., Hirama J., Nagasaka T., Ban-Ya S. (1991) Phase equilibria of liquid Fe-S-C ternary system. ISIJ International. 31, 1292-1299.

Withers AC., Bureau H., Raepsaet C., Hirschmann M., 2012. Calibration of infrared spectroscopy by elastic recoil analysis of H in synthetic olivine. Chemical Geology, 334, 92–98.

Wood, B.J., Walter, M.J., Wade, J., 2006. Accretion of the Earth and segregation of its core. Nature 441, 825–833.

Yang X., Keppler H., Li Y., 2016. Molecular hydrogen in mantle minerals. Geochem. Persp. Let., 2, 160-168.

Yagi T., Hishinuma T., 1995. Iron hydride formed by the reaction of iron, silicate, and water: implications for the light element of the Earth’s core. Geophys. Res. Lett. 22, 1933–1936.

Zhang Y. and Yin Q. Z., 2012. Carbon and other light element contents in the Earth’s core

based on first-principles molecular dynamics, Proceed. National Academy 109, 19579-19583.

Figure 1: ERDA measurements. MEB image of sample H4178 and the associated ERDA spectra for two areas of interest in metal (black) and silicate (gray) phases. The central metallic phase is surrounded by the silicate. H measurements have been made in regions of 200*200 μm^2 squares. ERDA spectra of the protons are presented for both phases, in normalized arbitrary units, as a function of the proton energy. The contaminated surface contribution in H can be clearly separated from the bulk signal, corresponding to the real H concentration of the phase.

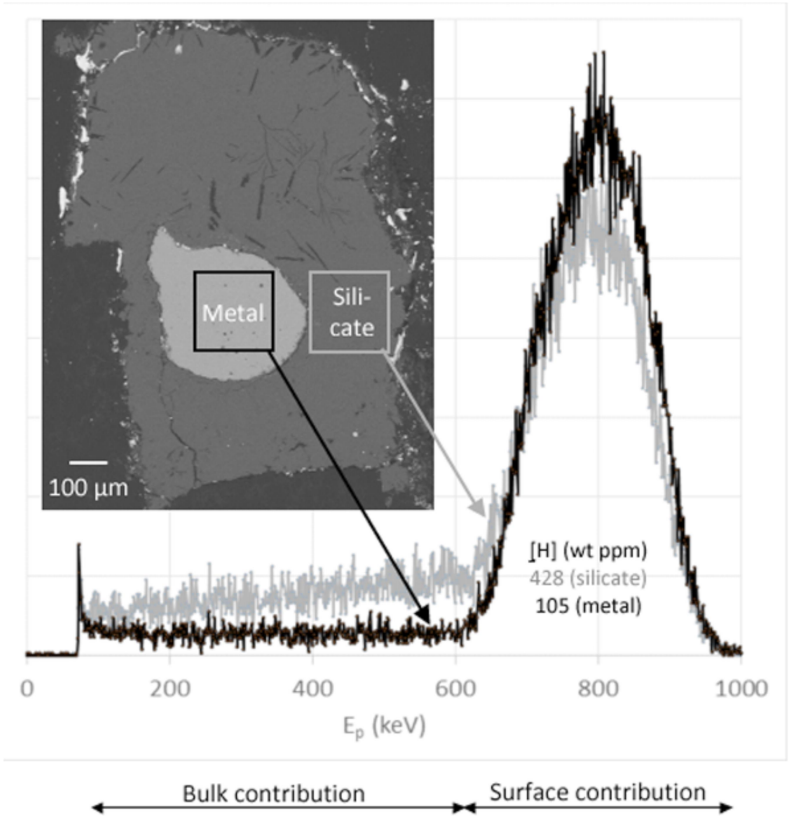

Figure 2: Raman spectra of the quenched silicate phases encountered in this study ((a) and (b)): (a) the starting H- and C-free anhydrous glass before the experiments and (b) the glass after the *HP-HT* experiments where the presence of H and C is obvious (see text for more details).

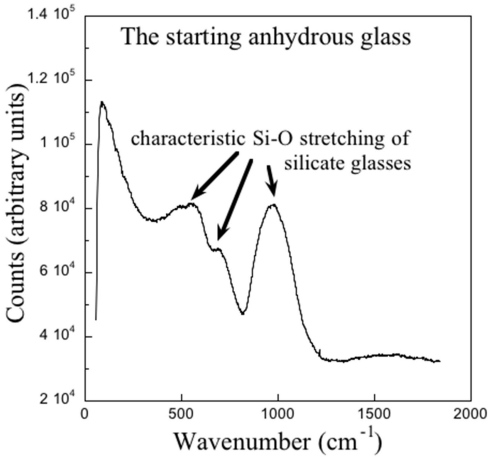

a

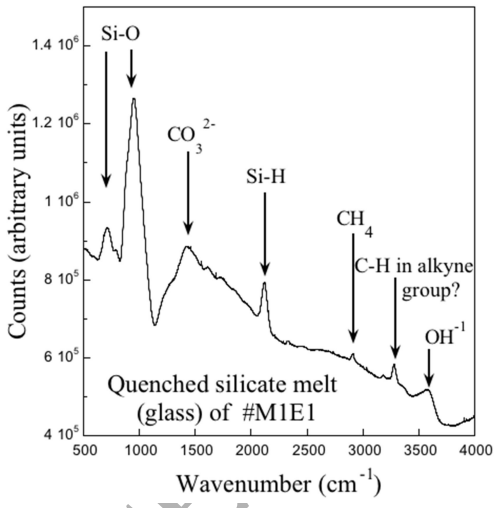

b

Figure 3: Scanning Electron Microscopy images of typical samples of this study:
(a) A multi-anvil sample (#H4178, 6 GPa and 1800°C). This sample is composed of two immiscible melts: a silicate and a Fe-Ni-rich metal; the graphite capsule is well visible. The quenched structures are much smaller than the size of the probes used for the analysis (EPMA, SIMS, ERDA and NRA). Zoom on the quenched metallic melts: "bubbles" (rounded dark shapes), linked to the presence of hydrogen in metal, may form during the quench as suggested and observed in previous works (*e.g.* Okuchi, 1997). (b) A multi-anvil brucite-free sample (#HV527, 5 GPa and 2200°C) composed of silicate and metal melts; the graphite capsule is also visible. Zoom on the quenched Fe-Ni-rich metal: there are numerous rods of graphite in the metal. No "bubble" is visible. The quenched silicate melt has tiny elongated structures.

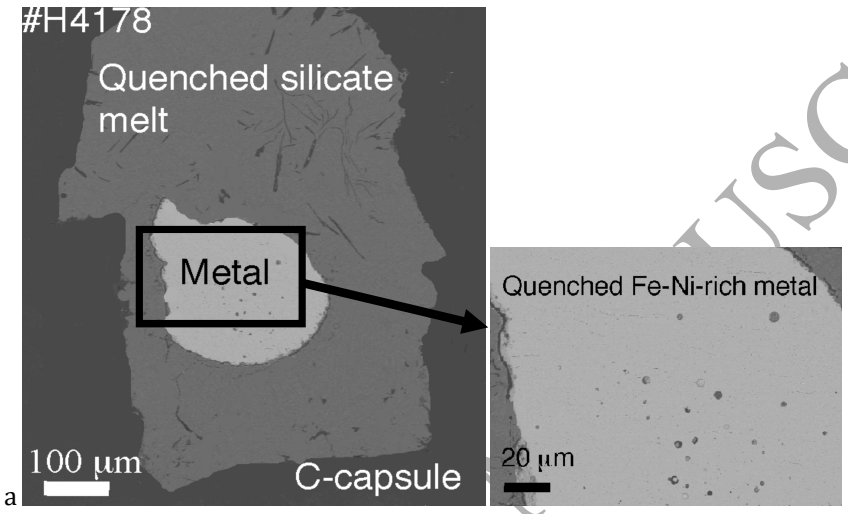

a

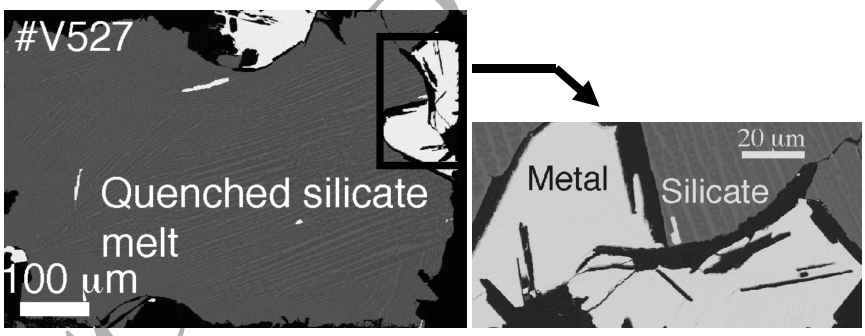

b

Figure 4: Partition coefficient of H ($D^{H}_{metal\text{-}silicate}$) between metal and silicate melts as a function of (a) oxygen fugacity relative to *IW* buffer (*ΔIW*), a linear regression line fitted the most oxidized data with a slope of 0.5. The other linear fits (with a slope of 1 and parallel to X-axis) were deduced from our Raman results and reactions (3), **(4), (5) and (6)** (see text for details); (b) *nbo/t*; (c) pressure, the two linear fits showed the lowest and highest pressure ranges for which $D^{H}_{metal\text{-}silicate}$ became siderophile; (d) temperature. These data confirm a linear decrease of $\log(D^{H}_{metal\text{-}silicate\ melt})$ with fO_2 and pressure. Our results are compared with literature data.

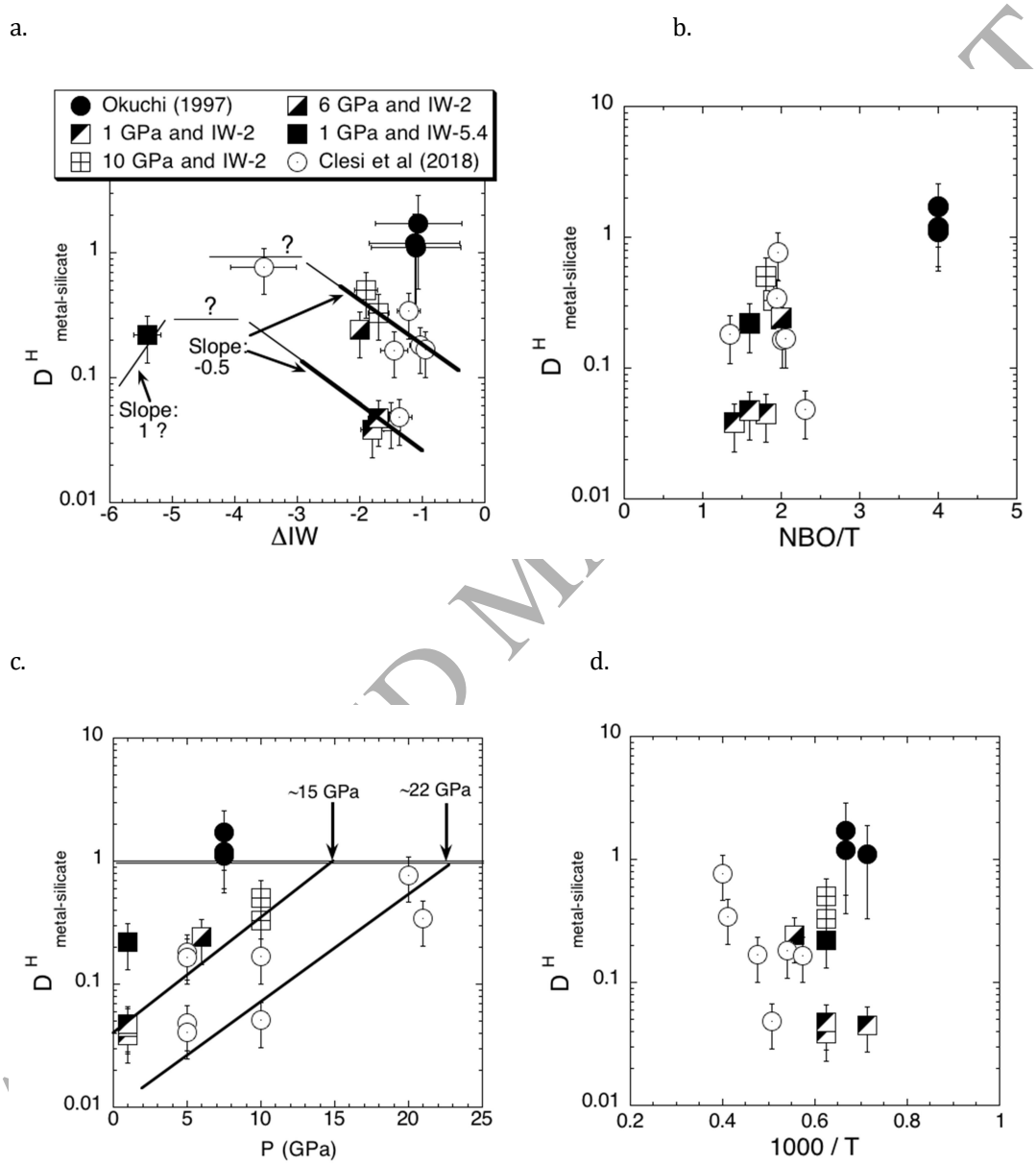

Figure 5 : Experimental partition coefficient of C ($D^{C}_{metal\text{-}silicate}$) between metal and silicate melts as a function of (a) oxygen fugacity relative to *IW* buffer (*ΔIW*) a regression line fitted our data with a slope of 0.5. The other data were fitted with the same slope. **Another slope might occur at lower fO_2 due to CH_4 formations (for example a slope parallel to *X*-axis might be deduced from reactions (6) see text for details)**; and (b) *nbo/t*; (c) pressure for which a linear trend (slope of 0.06) emerged for our *HP-HT* data; (d) temperature. Our results are compared with literature data.

a.

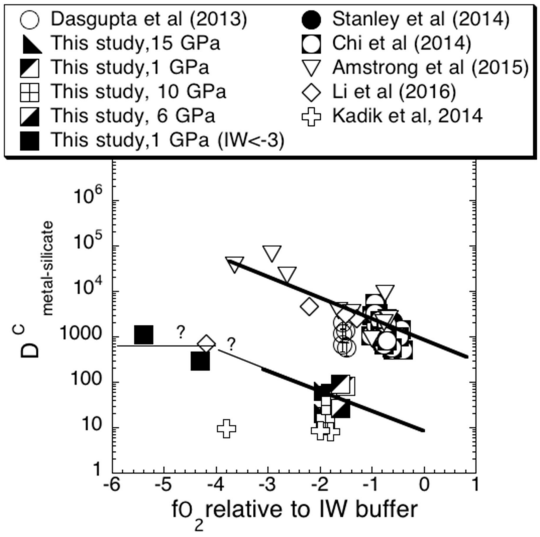

b.

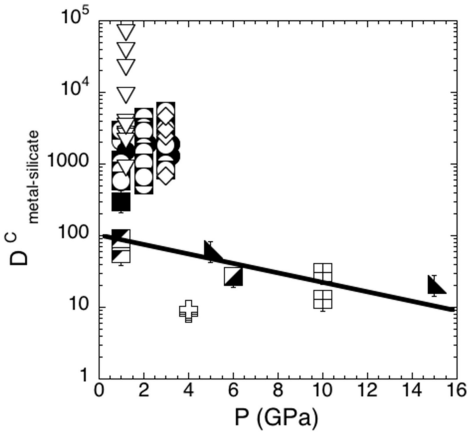

c.

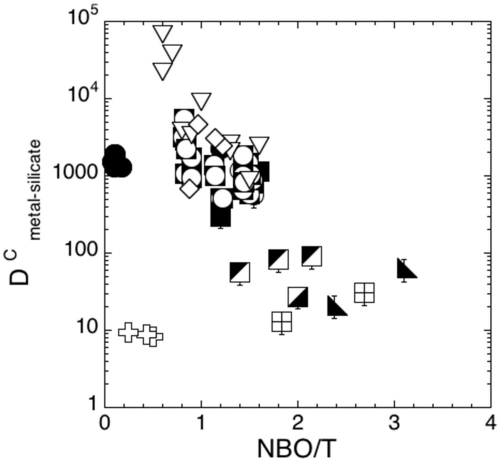

d.

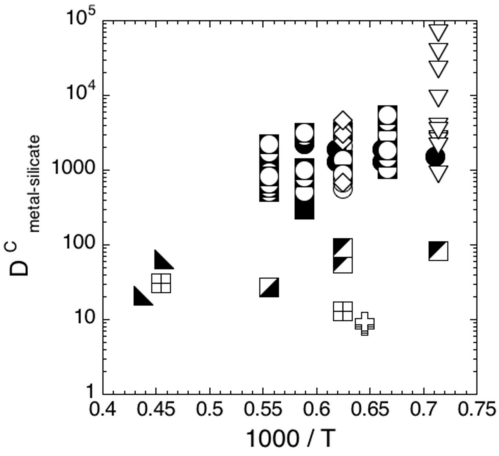

Figure 6: ($D^{H}_{metal\text{-}silicate}/^{DCmetal}_{\text{-}silicate}$) ratio obtained from our results as a function of pressure. The slope of the regression line was 0.22 and the correlation coefficient 0.97. This ratio showed no obvious trend with T, nbo/t and ΔIW.

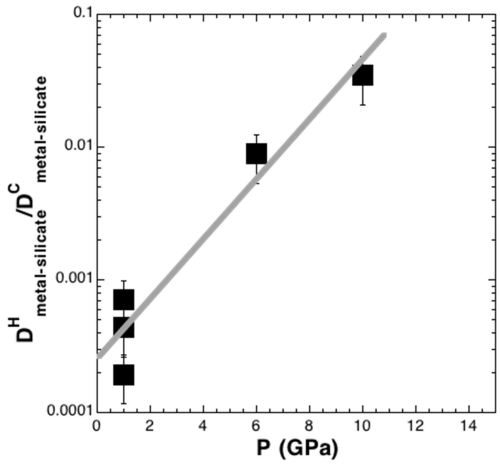

Table 1: Compositions of (A) the synthetic anhydrous glasses (in wt%, **EPMA** analysis) and (B) the metallic alloys used in the starting compositions of the present study (EPMA analysis).

A

	Glass 1	Glass 2	Wt%	Glass 1	Glass 2
Na	1.81 (±0.04)	-	Na_2O	2.44	-
Si	26.30 (±0.5)	23.70 (±0.5)	SiO_2	56.33	50.80
Al	2.91 (±0.06)	1.90 (±0.04)	Al_2O_3	5.49	3.60
K	0.32 (±0.01)	-	K_2O	0.39	-
Fe	8.21 (±0.23)	5.05 (±0.15)	FeO	10.56	6.50
Mg	12.58 (±0.26)	21.28 (±0.43)	MgO	20.78	35.30
Ca	1.98 (±0.06)	2.14 (±0.06)	CaO	2.77	3.00
Ti	0.29 (±0.035)	-	TiO_2	0.49	-
Cr	0.24 (±0.04)	0.10 (±0.02)	Cr_2O_3	0.36	0.14
Mn	0.21 (±0.04)	0.20 (±0.03)	MnO	0.27	0.15
O	45.15 (±0.50)	45.63	Total	99.97	99.49

B

	$Fe_{95}Ni_5$	$Fe_{90}Ni_5Si_5$	$Fe_{85}Ni_5Si_{10}$	$Fe_{99}Ni_1$
Fe	94.80 (±0.47)	90.20 (±0.45)	84.01 (±0.42)	98.08 (±0.50)
Ni	5.17 (±0.15)	4.54 (±0.13)	4.90 (±0.15)	1.87 (±0.07)
Si	-	5.20 (±0.18)	11.01 (±0.33)	-
Total	99.97	99.94	99.92	99.95

Table 2 : Experimental conditions and starting compositions.

Sample	P (GPa)	T (°C)	Run duration	Brucite in starting material (wt%)	Silicate in starting material and its proportion (wt%)	Metal in starting materials and its proportion (wt%)	H in starting material (wt%)*	H in the recovered sample (wt%)**	Fe in starting material (wt%)*	Fe in the recovered sample (wt%)**	Type of experiment	ΔIW (1)	ΔIW (2)
B1-10	10	1600	3 min	1.20	Glass 1 (72.60)	$Fe_{90}Ni_5Si_5$ (26.20)	0.041 (±0.006)	0.040 (±0.01)	29.6 (±0.9)	30.0 (±0.9)	MA	-1.7	-2.1
B2-10	10	1600	3 min	1.00	Glass 1 (78.00)	$Fe_{95}Ni_5$ (21.00)	0.034 (±0.005)	0.035 (±0.008)	26.4 (±0.9)	26.7 (±0.9)	MA	-1.6	-2.0
H4178	6	1800	2 min	0.76	Glass 1 (50.54)	$Fe_{95}Ni_5$ (48 .70)	0.026 (±0.004)	0.026 (±0.006)	50.4 (±0.8)	50.1 (±0.8)	MA	-1.5	-1.8
M6E2	1	1600	2 min	0.13	Glass 1 (49.77)	$Fe_{85}Ni_5Si_{10}$ (50.10)	0.0045 (±0.001)	0.0044 (±0.001)	46.6 (±0.7)	45.8 (±0.7)	PC	-5.2	-5.5
O1-16	1	1600	2 min	0.45	Glass 1 (54.15)	$Fe_{90}Ni_5Si_5$ (45.40)	0.015 (±0.003)	0.015 (±0.003)	47.6 (±0.8)	46.6 (±0.8)	PC	-1.5	-2.1
O1-14	1	1400	10 min	2.20	Glass 1 (53.60)	$Fe_{95}Ni_5$ (42.20)	0.076 (±0.01)	0.072 (±0.01)	46.4 (±0.8)	47.2 (±0.8)	PC	-1.4	-1.7
O2-16	1	1600	2 min	1.00	Glass 1 (62.00)	$Fe_{95}Ni_5$ (38.00)	0.035 (±0.005)	0.033 (±0.005)	41.0 (±0.8)	40.2 (±0.8)	PC	-1.7	-2.2
S4269	15	2300	3.5 min	0	Glass 2 (72.50)	$Fe_{99}Ni_1$ (27.50)	-	-	30.9 (±0.9)	30.8 (±0.8)	MA	-1.8	-2.3
S4270	10	2200	4 min	0	Glass 2 (72.50)	$Fe_{99}Ni_1$ (27.50)	-	-	30.8 (±0.9)	30.1 (±0.9)	MA	-1.8	-2.2
V527	5	2200	4 min	0	Glass 2 (72.50)	$Fe_{99}Ni_1$ (27.50)	-	-	30.9 (±0.9)	30.8 (±0.9)	MA	-1.8	-2.3
SB17	1	1600	30 min	0	Glass 2 (72.50)	$Fe_{95}Ni_5$ (27.50)	-	-	29.8 (±0.9)	30.3 (±0.9)	PC	-1.7	-2.1
SB21	1	1700	30 min	0	Glass 2 (72.50)	$Fe_{85}Ni_5Si_{10}$ (27.50)	-	-	27.0 (±0.9)	26.1 (±0.9)	PC	-4.1	-4.4

MA= multi anvil press ; PC= piston cylinder press ; ΔIW = fO_2 relative to IW buffer : (1) was calculated with activity coefficients or (2) with ideal behavior, see text for details: * H in the starting materials (before HT-HP run) was calculated from the proportion of brucite $Mg(OH)_2$ in the starting mixtures; ** H and Fe in the recovered sample were

calculated from a mass balance by using the proportion of each phase (metal and silicate melts) present in the sample and their H or Fe concentrations (given in the tables 3A and 3B).

Table 3: Sample **compositions.**

A. Silicate phase compositions (in wt%) obtained by EPMA, ERDA (for H, in ppm), SIMS (for C and H exclusively present as OH^-), NRA (for C). *H from ERDA and C from RNA were used for the partition coefficient calculations.*

Sample	*N*	Na_2O	MgO	Al_2O_3	SiO_2	K_2O	CaO	TiO_2	FeO	MnO	Cr_2O_3	Total*	H (ppm) *ERDA*	H (ppm) *SIMS*	C *RNA*	C *SIMS*
B1-10	15	1.36 (±0.03)	21.80 (±0.22)	2.39 (±0.03)	57.49 (±0.57)	-	3.87 (±0.06)	0.16 (±0.004)	11.52 (±0.11)	0.150 (±0.004)	0.260 (±0.008)	99.01	463 (±40)	430 (±40)	0.410 (±0.033)	0.520 (±0.05)
B2-10	15	1.18 (±0.03)	21.70 (±0.22)	3.89 (±0.06)	55.53 (±0.55)	0.24 (±0.007)	3.49 (±0.05)	0.53 (±0.0014)	12.60 (±0.12)	0.190 (±0.006)	0.16 (±0.005)	99.51	413 (±35)	440 (±44)	n.a.	0.170 (±0.02)
H4178	15	1.67 (±0.04)	21.39 (±0.21)	3.96 (±0.06)	53.55 (±0.53)	-	3.63 (±0.05)	-	15.18 (±0.15)	-	-	99.38	428 (±35)	350 (±45)	0.164 (±0.013)	0.149 (±0.02)
M6E2	25	1.85 (±0.04)	27.69 (±0.27)	4.63 (±0.06)	59.93 (±0.60)	0.48 (±0.012)	3.91 (±0.06)	0.31 (±0.008)	0.25 (±0.02)	0.120 (±0.004)	0.040 (±0.002)	99.21	72 (±7)	70 (±7)	0.0028 (±0.0003)	0.0020 (±0.0002)
O1-16	25	1.98 (±0.05)	22.83 (±0.22)	5.41 (±0.08)	49,87 (±0.50)	0.47 (±0.012)	4.11 (±0.06)	0.41 (±0.01)	14.28 (±0.14)	0.180 (±0.005)	0.230 (±0.007)	99.77	277 (±22)	n.a.	n.a.	n.a.
O1-14	25	1.65 (±0.04)	22.88 (±0.22)	4.91 (±0.07)	48.13 (±0.48)	0.48 (±0.012)	4.19 (±0.06)	0.41 (±0.01)	17.49 (±0.17)	0.170 (±0.005)	0.130 (±0.004)	99.84	1243 (±95)	1154 (±115)	0.030 (±0.003)	0.030 (±0.003)
O2-16	25	2.15 (±0.05)	21.72 (±0.21)	4.91 (±0.07)	54.83 (±0.55)	-	3.91 (±0.06)	0.38 (±0.01)	11.32 (±0.11)	0.200 (±0.006)	0.290 (±0.009)	99.71	529 (±44)	n.a.	0.05 (±0.007)	n.a.
4269	15	-	32.84 (±0.32)	3.73 (±0.06)	49.89 (±0.50)	-	2.91 (±0.05)	-	9.35 (±0.09)	0.400 (±0.01)	0.290 (±0.009)	99.41	-	-	0.25 (±0.02)	n.a.
4270	15	-	32.24 (±0.32)	3.93 (±0.06)	51.18 (±0.51)	-	3.35 (±0.05)	-	8.64 (±0.08)	-	-	99.34	-	-	0.23 (±0.02)	n.a.
V527	15	-	34.79 (±0.34)	3.74 (±0.05)	48.97 (±0.50)	-	2.93 (±0.04)	-	9.07 (±0.09)	0.320 (±0.01)	-	99.82	-	-	0.07 (±0.007)	n.a.
SB17	20	0.35 (±0.008)	28.29 (±0.28)	1.98 (±0.03)	54.88 (±0.55)	-	1.85 (±0.03)	-	11.44 (±0.11)	0.400 (±0.01)	0.59 (±0.02)	99.78	-	-	0.04 (±0.004)	n.a.
SB21	20	0.67 (±0.02)	26.46 (±0.24)	2.32 (±0.03)	67.69 (±0.67)	-	1.59 (±0.03)	-	0.79 (±0.08)	0.320 (±0.01)	0.100 (±0.003)	99.94	-	-	0.02 (±0.0018)	n.a.

- : **values below** detection limit ; n.a. : not analyzed ;* Total without the contribution of SIMS, ERDA and RNA analysis ; *N* is the number of EPMA measurements averaged to obtain the composition

reported.

B. Metal compositions (in wt%) obtained by EPMA, ERDA (for H, in ppm), NRA (for C) and SEM-EDS.

Sample	*N*	Fe	Ni	Si	Pt	Cr	Total*	C *RNA*	H (ppm) *ERDA*
B1-10	10	90.03 (±0.40)	5.46 (±0.09)	0.02 (±0.002)	0.09 (±0.01)	0.03 (±0.003)	95.63	4.34 (±0.11)	236 (±22)
B2-10	10	91.20 (±0.42)	6.40 (±0.10)	0.03 (±0.003)	-	0.01 (±0.001)	97.64	n.a.	137 (±13)
H4178	10	90.70 (±0.42)	4.85 (±0.08)	-	-	-	95.55	4.45 (±0.11)	105 (±10)
M6E2	12	91.10 (±0.42)	3.30 (±0.05)	2.00 (±0.20)	-	0.21 (±0.02)	96.61	3.41 (±0.09)	16 (±2)
O1-16	12	89.20 (±0.40)	4.50 (±0.07)	0.01 (±0.001)	3.60 (±0.20)	0.04 (±0.004)	97.35	n.a.	13 (±2)
O1-14	10	90.50 (±0.40)	5.13 (±0.08)	0.01 (±0.001)	0.20 (±0.02)	0.06 (±0.006)	95.90	4.10 (±0.10)	56 (±6)
O2-16	10	91.40 (±0.41)	5.22 (±0.08)	0.01 (±0.001)	-	0.04 (±0.004)	96.67	3.39 (±0.10)	20 (±2.5)
4269	10	93.00 (±0.43)	1.20 (±0.02)	-	0.19 (±0.02)	0.20 (±0.02)	94.59	5.20 (±0.13)	-
4270	10	91.45 (±0.41)	1.13 (±0.03)	-	-	0.30 (±0.04)	92.88	7.07 (±0.14)	-
V527	10	93.70 (±0.43)	1.51 (±0.03)	-	0.19 (±0.02)	0.20 (±0.02)	95.60	4.41 (±0.11)	-
SB17	10	90.40 (±0.40)	5.59 (±0.08)	0.04 (±0.005)	-	0.37 (±0.04)	93.87	3.60 (±0.11)	-
SB21	10	87.94 (±0.38)	4.50 (±0.07)	1.13 (±0.11)	-	0.30 (±0.04)	99.47	5.60 (±0.13)	-

- : values below detection limit ;* Total without the contribution of ERDA and RNA analysis.
N is the number of EPMA measurements averaged to obtain the composition reported.

Table 4 : Partition coefficients of H and Fe between metal and quenched silicate melts obtained in this study.

Sample	P (GPa)	T (°C)	ΔIW (fO_2 relative to IW buffer)	NBO/T	$D^{Fe}_{metal/silicate}$	$D^{C}_{metal/silicate}$	$D^{H}_{metal/silicate}$
B1-10	10	1600	-1.7	1.8	**10.0** (±0.5)	**10.6** (±1.5)	**0.50** (±0.10)
B2-10	10	1600	-1.6	1.9	**9.4** (±0.5)	-	**0.33** (±0.07)
H4178	6	1800	-1.5	2.0	**7.7** (±0.4)	**27** (±2.5)	**0.24** (±0.06)
M6E2	1	1600	-5.2	1.6	**455** (±18)	**1137** (±100)	**0.22** (±0.06)
O1-16	1	1600	-1.5	1.6	**8.0** (±0.4)	-	**0.047** (±0.012)
O2-16	1	1600	-1.7	1.4	**10.4** (±0.5)	**68** (±9)	**0.038** (±0.01)
O1-14	1	1400	-1.4	1.8	**6.65** (±0.4)	**137** (±12.5)	**0.045** (±0.012)
S4269	15	2300	-1.8	2.4	**12.8** (±0.7)	**21.0** (±2)	-
S4270	10	2200	-1.8	2.7	**13.6** (±0.5)	**30.7** (±3)	-
V527	5	2200	-1.8	3.1	**13.2** (±0.7)	**63** (±6)	-
SB17	1	1600	-1.7	2.1	**10.1** (±0.5)	**90** (±6)	-
SB21	1	1700	-4.1	1.2	**140** (±0.7)	**280** (±26)	-

$D^{X}_{metal\text{-}silicate}$ is the partition coefficient of X (= C, Fe or H) between metallic and silicate melts and derived by dividing the concentration of element X (by weight) in metallic melt by its concentration (by weight) in silicate melt.